



PAPER • OPEN ACCESS

Hidden Weyl points in centrosymmetric paramagnetic metals

To cite this article: Dominik Gresch *et al* 2017 *New J. Phys.* **19** 035001

View the [article online](#) for updates and enhancements.

Related content

- [Topological semimetals predicted from first-principles calculations](#)
- [Topological Weyl semimetals in the chiral antiferromagnetic materials \$\text{Mn}_3\text{Ge}\$ and \$\text{Mn}_3\text{Sn}\$](#)
- [Spin-mixing-tunneling network model for Anderson transitions in two-dimensional disordered spinful electrons](#)

Recent citations

- [Spin-lattice relaxation phenomena in the magnetic state of a suggested Weyl semimetal \$\text{CeAlGe}\$](#)
Karan Singh and K. Mukherjee
- [Zeeman-splitting-induced topological nodal structure and anomalous Hall conductivity in \$\text{ZrTe}_5\$](#)
Yichul Choi *et al*
- [Topological crystalline insulator state with type-II Dirac fermions in transition metal dipnictides](#)
Baokai Wang *et al*



PAPER

Hidden Weyl points in centrosymmetric paramagnetic metals

Dominik Gresch^{1,3}, QuanSheng Wu¹, Georg W Winkler¹ and Alexey A Soluyanov^{1,2}¹ Theoretical Physics and Station Q Zurich, ETH Zurich, 8093 Zurich, Switzerland² Department of Physics, St Petersburg State University, St Petersburg, 199034 Russia³ Author to whom any correspondence should be addressed.E-mail: greschd@phys.ethz.ch

Keywords: Weyl semimetal, chiral anomaly, magnetoresistance, Zeeman splitting

RECEIVED

6 November 2016

REVISED

17 January 2017

ACCEPTED FOR PUBLICATION

2 February 2017

PUBLISHED

2 March 2017

Original content from this work may be used under the terms of the [Creative Commons Attribution 3.0 licence](#).

Any further distribution of this work must maintain attribution to the author(s) and the title of the work, journal citation and DOI.



Abstract

The transition metal dipnictides TaAs₂, TaSb₂, NbAs₂ and NbSb₂ have recently sparked interest for exhibiting giant magnetoresistance. While the exact nature of the magnetoresistance in these materials is still under active investigation, there are experimental results indicating that it is of the anisotropic negative variety. We study the effect of magnetic fields on the band structure topology of these materials by applying Zeeman splitting. In the absence of a magnetic field, we find that the materials are weak topological insulators, which is in agreement with previous studies. When the magnetic field is applied, we find that type-II Weyl points form. This result is found first from a symmetry argument, and then numerically for a $\mathbf{k} \cdot \mathbf{p}$ model of TaAs₂ and a tight-binding model of NbSb₂. This effect could be of help in the search for an explanation of the anomalous magnetoresistance in these materials.

1. Introduction

Weyl nodes are the point-like crossings of two energy bands with linear dispersion. Locally, they can be described by a Hamiltonian of the form

$$\mathcal{H}(\mathbf{k}) = \sum_{i,j} k_i A_{i,j} \sigma_j \quad (1)$$

where $i \in \{x, y, z\}$ and $j \in \{0, x, y, z\}$. Topologically, a Weyl node can be characterized as being a quantized source or sink of Berry curvature, depending on its chirality [1]. Due to their quantized nature, Weyl points can only be created or annihilated in pairs of opposite chirality.

It was recently shown [2] that Weyl nodes come in two types. Type-I Weyl fermions have a point-like Fermi surface. When a magnetic field is applied, they exhibit a chiral Landau level [3–5] regardless of the magnetic field direction. When this chiral Landau level crosses the Fermi level, it can be a source of reduced magnetoresistance [6–11]. Type-II Weyl fermions, on the other hand, have an energy spectrum that is tilted by a strong σ_0 contribution to the Hamiltonian (equation (1)). As a consequence, the Fermi surface opens, and the chiral anomaly is anisotropic, appearing only for certain magnetic field directions.

The inversion symmetry P maps a Weyl node at point \mathbf{k} onto a Weyl node of opposite chirality at $-\mathbf{k}$. Similarly, the time-reversal symmetry \mathcal{T} maps a Weyl point at \mathbf{k} onto one at $-\mathbf{k}$, but without changing its chirality. Consequently, in the presence of the product symmetry $\mathcal{T} * P$, Weyl nodes are mapped onto themselves but with opposite chirality. This four-fold degenerate crossing, consisting of two superimposed Weyl points of opposite chirality, is known as a Dirac node. Unlike Weyl points, they are not protected from gapping by any quantized topological charge. Consequently, additional symmetries are needed to stabilize Dirac nodes.

In centrosymmetric non-magnetic materials, the presence of both inversion and time-reversal symmetry only allows for Dirac nodes to form. Weyl nodes are not possible unless the product symmetry $\mathcal{T} * P$ is broken.

Recently, transition metal dipnictides of the type AB₂ ($A \in \{\text{Ta}, \text{Nb}\}$, $B \in \{\text{As}, \text{Sb}\}$) have gained a lot of attention [12–19] for their giant magnetoresistance. These materials are semimetals, but without a direct closure of the band gap. Consequently, they do not host any Weyl or Dirac points.

Table 1. Unit cell dimensions (in Å) for AB₂ compounds.

	a	b	c	d
TaAs₂	4.6655	1.6915	3.8420	6.7330
TaSb₂	5.11	1.822	4.1950	7.1502
NbAs₂	4.684	1.698	3.8309	6.7933
NbSb₂	5.1198	1.8159	4.1705	7.2134

Table 2. Atomic positions (*x*, *y*).

	A	B1	B2
TaAs₂	(0.157, 0.1959)	(0.4054, 0.1082)	(0.1389, 0.5265)
TaSb₂	(0.152, 0.19)	(0.405, 0.113)	(0.147, 0.535)
NbAs₂	(0.1574, 0.1965)	(0.4059, 0.1084)	(0.14, 0.528)
NbSb₂	(0.1521, 0.1903)	(0.4051, 0.1127)	(0.1475, 0.5346)

The exact nature of magnetoresistance in these materials—especially the dependency on the direction of the magnetic field—is still under active investigation. Negative magnetoresistance has been observed experimentally for NbAs₂ [17, 18], TaAs₂ [17] and TaSb₂ [17, 20]. Anomalous, albeit not negative, magnetoresistance has been observed for NbSb₂ [12] and TaAs₂ [15]. However, there are also experiments which point to the opposite, which is that there is no negative magnetoresistance in these materials. In [16], negative magnetoresistance was observed at first, but was then determined to be an artifact of the measurement setup.

In the following, we propose a mechanism for Weyl nodes to appear in these materials under the influence of a magnetic field. The chiral anomaly associated with these Weyl nodes is a possible source of negative magnetoresistance. Such an appearance of Weyl points under a magnetic field has recently been proposed in [21]. The mechanism with which the Weyl points appear, however, is a different one: in this work, the Weyl points appear from a previously gapped state, while [21] discusses Weyl points arising from the splitting of a four-fold crossing.

The paper is structured as follows: in the first section, the atomic and electronic structure of the four compounds is described. A four-band Hamiltonian for TaAs₂ is derived from the symmetry considerations and fitted to the band structure. In the second section, the topology of the band structure is studied, first without a magnetic field and then by applying a Zeeman term. We find that this leads to the appearance of Weyl points.

2. Atomic and electronic structure of AB₂ compounds

2.1. Atomic structure

In the following, the atomic structure of TaAs₂ [22], TaSb₂ [23], NbSb₂ [24] and NbAs₂ [25] is described.

The reduced unit cell of AB₂ compounds has the general form

$$\begin{aligned} a_1 &= (a, b, 0) \\ a_2 &= (-a, b, 0) \\ a_3 &= (-c, 0, d) \end{aligned} \quad (2)$$

with the parameters as given in table 1 [22, 24].

Each unit cell contains two formula units. The atoms are located at the general Wyckoff positions (*x*, −*x*, *y*) and (−*x*, *x*, −*y*) for (*x*, *y*), as shown in table 2 [22, 24].

Figure 1 shows the reduced unit cell and first BZ of TaAs₂. The *k*-point path along which the bandstructure calculations are performed is indicated. On the basis reciprocal to that of equation (2), the special *k*-points are given by

$$\begin{aligned} \Gamma &= (0, 0, 0) \\ A &= (0, 0, 0.5) \\ L &= (0.5, 0, 0.5) \\ M &= (0.5, 0.5, 0.5) \\ V &= (0.5, 0, 0) \\ Y &= (0.5, 0.5, 0). \end{aligned} \quad (3)$$

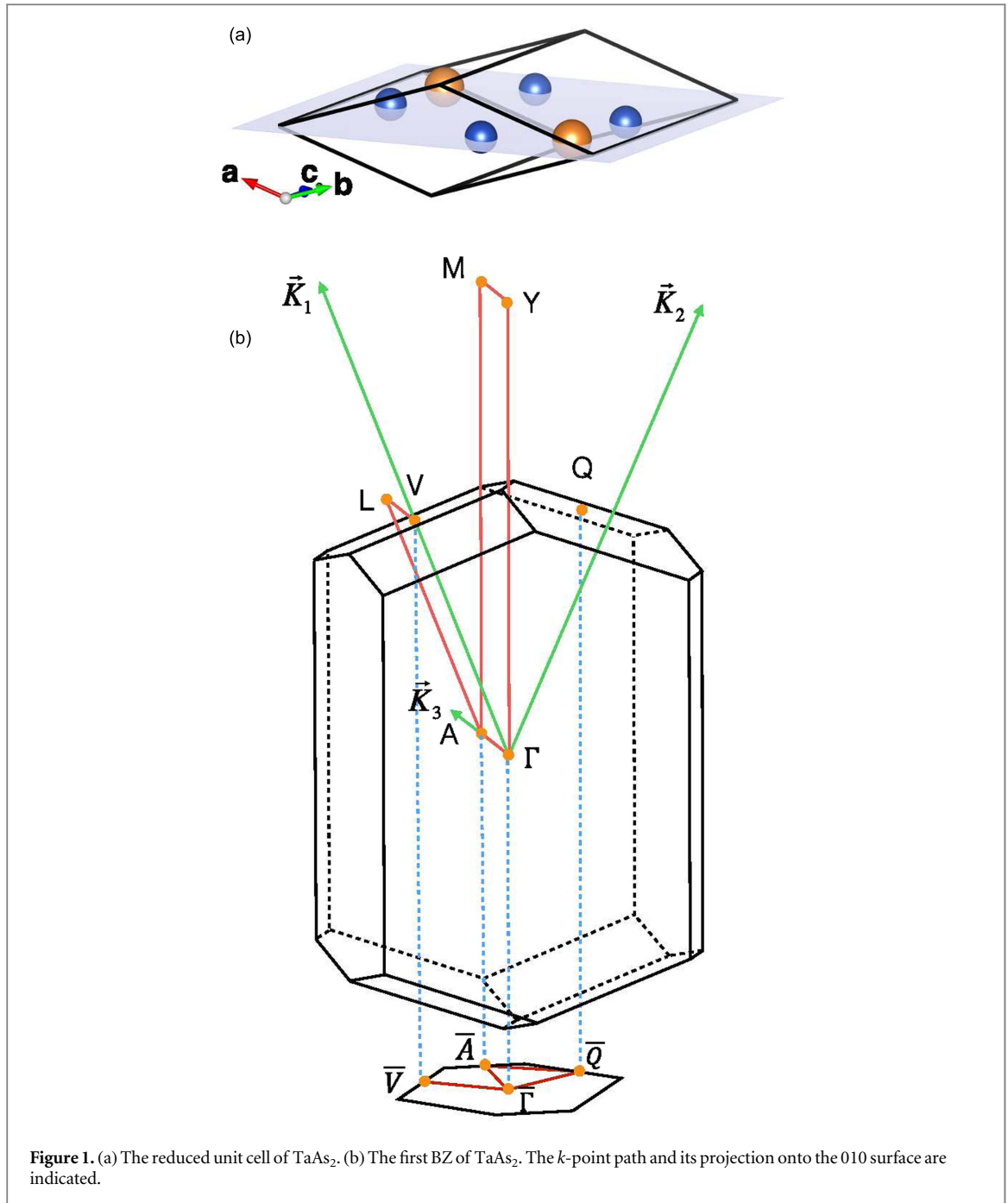


Figure 1. (a) The reduced unit cell of TaAs₂. (b) The first BZ of TaAs₂. The *k*-point path and its projection onto the 010 surface are indicated.

2.2. Electronic structure

The electronic structure calculations were performed in VASP [26], with the projector augmented-wave (PAW) [27, 28] pseudopotentials. The PBE approximation [29] was used, and spin–orbit coupling was included in the potentials. The self-consistent field (SCF) calculations were performed on a $11 \times 11 \times 5$ Γ -centered grid for TaAs₂, and a $10 \times 10 \times 5$ Γ -centered grid for NbSb₂. The energy cut-off given in the potential files was used, which is 293.2 eV for NbAs₂ and NbSb₂, and 223.7 eV for TaAs₂ and TaSb₂.

Additionally, the PBE calculations were tested against the accurate HSE06 hybrid functional [30, 31]. The hybrid SCF calculations for the band structures were performed on a Γ -centered $6 \times 6 \times 4$ grid for all materials. For the generation of the Wannier tight-binding model of NbSb₂, a Γ -centered $10 \times 10 \times 5$ grid was used.

The band structure of TaAs₂ and NbSb₂ is shown in figure 2. Both materials exhibit a pair of electron and hole pockets near the *M*-point, where the minimum band gap is about 318 meV (120 meV without hybrid functionals) in the case of TaAs₂, 151 meV (98 meV) for TaSb₂, 261 meV (22 meV) for NbAs₂, and 67 meV (18 meV) in the case of NbSb₂. A more complete calculation of the band structure can be found, for example, in [32].

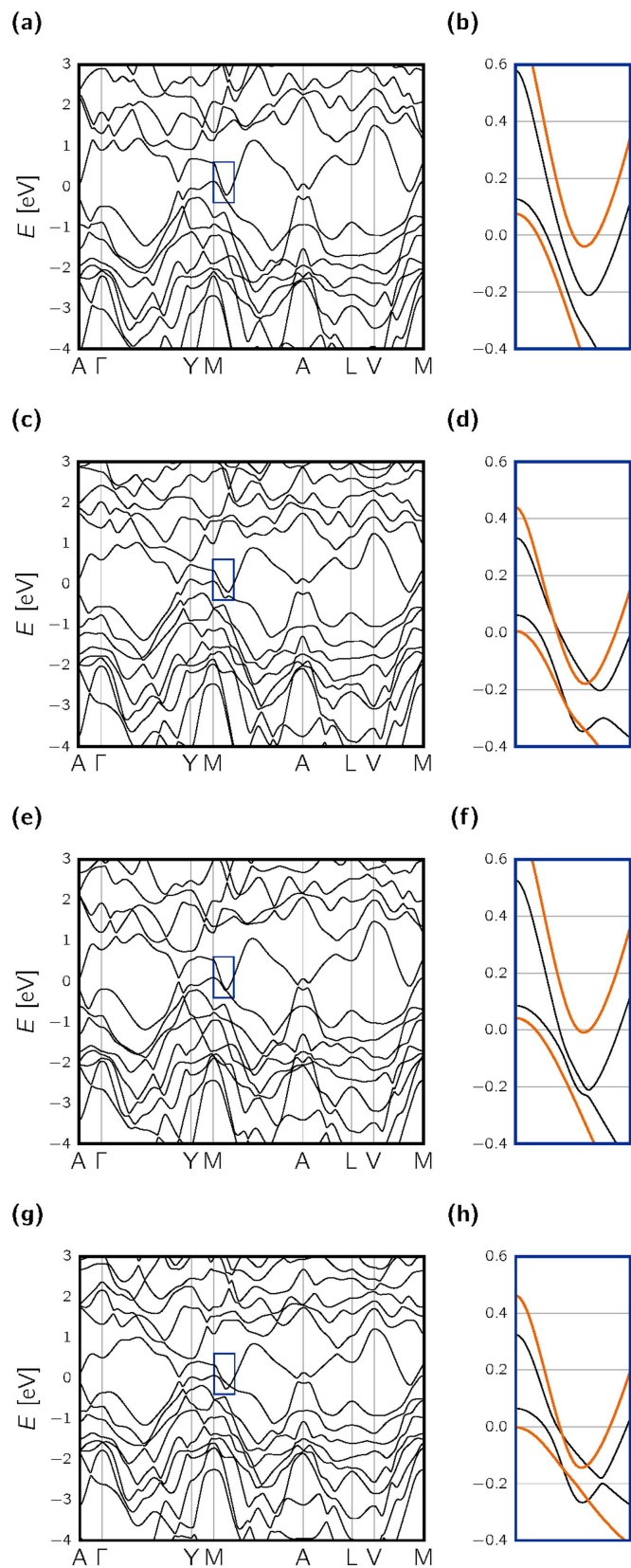


Figure 2. The band structures of AB_2 compounds. The inset shows electron and hole pockets around M . The orange line represents the calculations using hybrid functionals. (a and b) $TaAs_2$, (c and d) $TaSb_2$, (e and f) $NbAs_2$, (g and h) $NbSb_2$.

2.3. Symmetry operations and the $\mathbf{k} \cdot \mathbf{p}$ model

The AB_2 compounds studied here have $C2/m$ symmetry (space group 12). The rotation axis is along the Cartesian y -axis. In reduced coordinates, the symmetry matrices are as follows:

Table 3. Character table for the relevant double group representations of C_{2m} [33].

	E	C_{2y}	P	M_y
Γ_3^+	1	i	1	i
Γ_4^+	1	$-i$	1	$-i$
Γ_3^-	1	i	-1	$-i$
Γ_4^-	1	$-i$	-1	i

- Identity $E = \mathbb{I}_{3 \times 3}$
- Rotation $C_{2y} = \begin{pmatrix} 0 & 1 & 0 \\ 1 & 0 & 0 \\ 0 & 0 & -1 \end{pmatrix}$
- Parity $P = -\mathbb{I}_{3 \times 3}$
- Mirror $M_y = PC_{2y} = \begin{pmatrix} 0 & -1 & 0 \\ -1 & 0 & 0 \\ 0 & 0 & 1 \end{pmatrix}$.

From the first-principles wave-functions, the representations corresponding to the two highest valence and two lowest conduction bands at the M -point were determined using the WIEN2k code [34, 35]. They were found to be Γ_3^+ , Γ_4^+ and Γ_3^- , Γ_4^- , respectively. Their characters are shown in table 3, which comes from table 15 on page 35 in Koster *et al* [33]. Consequently, the symmetry representations in these four bands are given by

- Identity $E = \mathbb{I}_{4 \times 4}$
- Rotation $C_{2y} = \begin{pmatrix} i & 0 & 0 & 0 \\ 0 & -i & 0 & 0 \\ 0 & 0 & i & 0 \\ 0 & 0 & 0 & -i \end{pmatrix}$
- Parity $P = \begin{pmatrix} 1 & 0 & 0 & 0 \\ 0 & 1 & 0 & 0 \\ 0 & 0 & -1 & 0 \\ 0 & 0 & 0 & -1 \end{pmatrix}$
- Mirror $M_y = PC_{2y} = \begin{pmatrix} i & 0 & 0 & 0 \\ 0 & -i & 0 & 0 \\ 0 & 0 & -i & 0 \\ 0 & 0 & 0 & i \end{pmatrix}$
- Time-reversal $\mathcal{T} = \begin{pmatrix} 0 & -1 & 0 & 0 \\ 1 & 0 & 0 & 0 \\ 0 & 0 & 0 & -1 \\ 0 & 0 & 1 & 0 \end{pmatrix} \hat{K}$.

For each of the symmetry operations g , the constraint

$$\mathcal{H}(\mathbf{k}) = D(g)\mathcal{H}(g^{-1}\mathbf{k})D(g^{-1}) \quad (4)$$

is imposed on the 4×4 Hamiltonian, where $D(g)$ is the symmetry representation. By applying these constraints on the general form of a four-band Hamiltonian

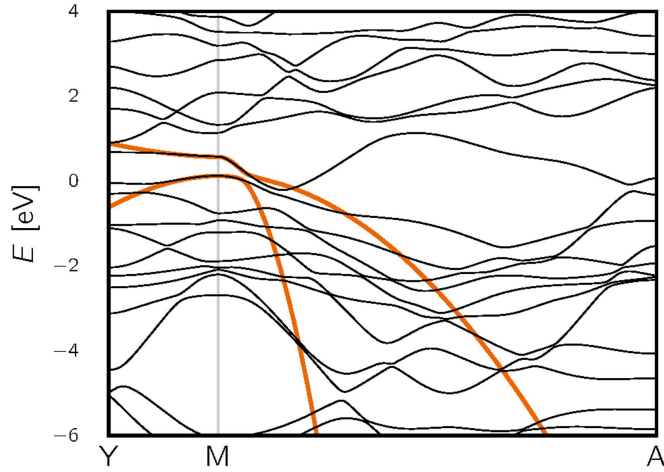
$$\mathcal{H}(\mathbf{k}) = \sum_{i,j \in \{0,x,y,z\}} C_{ij}(\mathbf{k})(\sigma_i \otimes \sigma_j), \quad (5)$$

we find the Hamiltonian to be of the form

$$\begin{aligned} \mathcal{H}(\mathbf{k}) = & C_{00}(\mathbf{k})(\sigma_0 \otimes \sigma_0) + C_{xx}(\mathbf{k})(\sigma_x \otimes \sigma_x) \\ & + C_{xy}(\mathbf{k})(\sigma_x \otimes \sigma_y) + C_{xz}(\mathbf{k})(\sigma_x \otimes \sigma_z) \\ & + C_{y0}(\mathbf{k})(\sigma_y \otimes \sigma_0) + C_{z0}(\mathbf{k})(\sigma_z \otimes \sigma_0), \end{aligned} \quad (6)$$

Table 4. Parameters of the 4×4 Hamiltonian of TaAs₂ around M up to the second order.

[eV]	C_{00}^1	$= 7.066$	C_{z0}^1	$= -0.224$
[eVÅ]	C_{xz}^{x+y}	$= 1.272$	C_{y0}^{x+y}	$= 1.270$
	C_{xx}^{x-y}	$= -0.061$	C_{xy}^{x-y}	$= -1.999$
	C_{xx}^z	$= -0.554$	C_{xy}^z	$= -0.253$
[eVÅ ²]	$C_{00}^{x^2+y^2}$	$= -71.21$	$C_{z0}^{x^2+y^2}$	$= 56.30$
	C_{00}^{xy}	$= -137.1$	C_{z0}^{xy}	$= 123.1$
	C_{00}^{xz-yz}	$= 1.52$	C_{z0}^{xz-yz}	$= -1.49$
	C_{00}^z	$= -0.84$	C_{z0}^z	$= -1.88$

**Figure 3.** The TaAs₂ band structure of the $\mathbf{k} \cdot \mathbf{p}$ model (thick orange line), compared to the first-principles result (black lines).

where the $C_{ij}(\mathbf{k})$ are given up to the second order in $\mathbf{k}^* = \mathbf{k} - M$ (in reduced coordinates) by

$$C_{00}(\mathbf{k}^*) = C_{00}^1 + C_{00}^{x^2+y^2}((k_x^*)^2 + (k_y^*)^2) + C_{00}^{xy} k_x^* k_y^* + C_{00}^{xz-yz}(k_x^* k_z^* - k_y^* k_z^*) + C_{00}^{z^2} (k_z^*)^2 \quad (7)$$

$$C_{z0}(\mathbf{k}^*) = C_{z0}^1 + C_{z0}^{x^2+y^2}((k_x^*)^2 + (k_y^*)^2) + C_{z0}^{xy} k_x^* k_y^* + C_{z0}^{xz-yz}(k_x^* k_z^* - k_y^* k_z^*) + C_{z0}^{z^2} (k_z^*)^2 \quad (8)$$

$$C_{xx}(\mathbf{k}^*) = C_{xx}^{x-y}(k_x^* - k_y^*) + C_{xx}^z k_z^* \quad (9)$$

$$C_{xy}(\mathbf{k}^*) = C_{xy}^{x-y}(k_x^* - k_y^*) + C_{xy}^z k_z^* \quad (10)$$

$$C_{xz}(\mathbf{k}^*) = C_{xz}^{x+y}(k_x^* + k_y^*) \quad (11)$$

$$C_{y0}(\mathbf{k}^*) = C_{y0}^{x+y}(k_x^* + k_y^*). \quad (12)$$

These 16 parameters were numerically fitted to the band structure of TaAs₂ using the `SciPy` [36] package to obtain the values in table 4. The resulting band structure around the M -point is shown in figure 3. Comparing it to the band structure obtained from first-principles reveals that the approximation is accurate in the immediate vicinity of the M -point, but breaks down at around 6% of the distance along the line M – A . Importantly, the minimum band gap is not preserved in this model. Nevertheless, the model can be used to qualitatively study effects in TaAs₂, owing to the fact that it contains the correct symmetry representations.

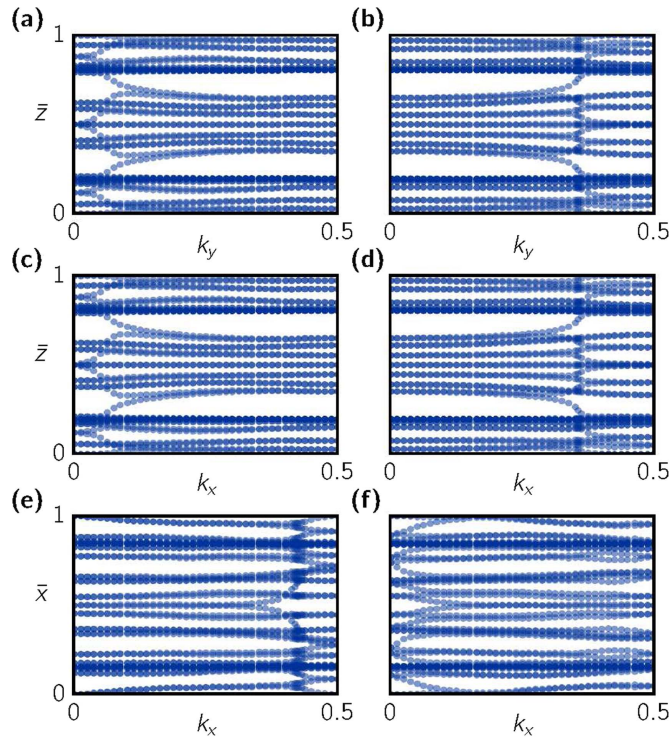


Figure 4. The Wannier charge center evolution for the time-reversal invariant planes of TaAs₂. (a) $k_x = 0$, (b) $k_x = 0.5$, (c) $k_y = 0$, (d) $k_y = 0.5$, (e) $k_z = 0$ and (f) $k_z = 0.5$.

3. Band structure topology

In this section, we describe the band structure topology and the influence of the magnetic field. First, we describe the topology in the absence of the magnetic field for all four compounds. Then, we show that Weyl points appear under a sufficient magnetic field. This result is shown first for the $\mathbf{k} \cdot \mathbf{p}$ model of TaAs₂ derived in section 2.3, and then for a tight-binding model of NbSb₂ derived from first-principles.

3.1. Band structure topology without magnetic fields

In the absence of a magnetic field, there is no direct band gap closure in AB₂ compounds. Since the valence bands thus form a well-defined manifold, they can be classified, just like insulators, according to the topology of these valence bands. Because time-reversal symmetry is fulfilled, a \mathbb{Z}_2 classification is possible.

All compounds were found to be weak topological insulators, with \mathbb{Z}_2 indices 0; (111). That is, all time-reversal invariant planes $k_i = 0, 0.5$ have a non-trivial \mathbb{Z}_2 index $\Delta = 1$. This result was derived from first-principles using the Z2Pack code [37], and agrees with previous studies [15, 17, 32]. The corresponding evolution of the Wannier charge centers is shown, for the case of TaAs₂, in figure 4.

Figure 5 shows the surface density of states for a slab of TaAs₂, with surfaces parallel to the mirror plane perpendicular to the Cartesian y -axis (the light blue plane shown in figure 1). The presence of topological surface states confirms the conclusion that the material is a weak topological insulator. The surface spectrum was calculated by the iterative Green's function [38], which was implemented in WannierTools [39].

3.2. The effect of Zeeman splitting on the $\mathbf{k} \cdot \mathbf{p}$ model for TaAs₂

Here we study the effects of the magnetic field on TaAs₂ by adding a Zeeman splitting term to the $\mathbf{k} \cdot \mathbf{p}$ model derived in section 2.3 (equation (6)). The splitting term is given by

$$\Delta\mathcal{H} = c_x \sigma_0 \otimes \sigma_y + c_y \sigma_0 \otimes \sigma_z + c_z \sigma_0 \otimes \sigma_x, \quad (13)$$

where c_i is the strength of the Zeeman splitting induced by the magnetic field in that direction, that is

$$c_i = \sum_j g_{ij} \mu_B H_j. \quad (14)$$

This assumes that the g -factor is equal for all bands. The limitations of this approximation are discussed in section 3.4.

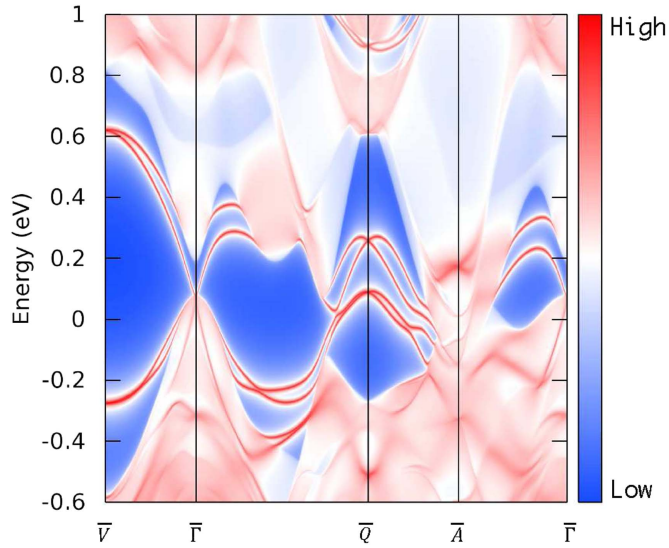


Figure 5. The surface density of states of TaAs₂ on the 010 surface, along the k -point path shown in figure 1.

3.2.1. Magnetic field along the rotation axis \hat{y}

When a magnetic field is applied along the rotation axis \hat{y} , the Zeeman term equation (13) takes the form

$$\Delta\mathcal{H} = c_y \sigma_0 \otimes \sigma_z. \quad (15)$$

This term preserves all spatial symmetries of the system, breaking only time-reversal.

Along the M – A line, the C_{xx} and C_{yy} contributions to the Hamiltonian vanish since $k_x^* = k_y^*$ and $k_z^* = 0$. Consequently, the energy eigenvalues are given by

$$E(\mathbf{k}) = C_{00}(\mathbf{k}) \pm c_y \mp \sqrt{C_{xz}(\mathbf{k})^2 + C_{y0}(\mathbf{k})^2 + C_{z0}(\mathbf{k})^2}. \quad (16)$$

The Zeeman term counteracts the original splitting (square root term), such that for a sufficient magnetic field there will be a direct band gap closure. Away from the M – A line, the band gap remains open, giving rise to a Weyl point.

When the Zeeman splitting is gradually switched on, two pairs of Weyl points form at about $c_y = 0.11$ eV. Increasing the Zeeman splitting leads to a separation between the two nodes in a pair, with one node each moving towards the M -point. Finally, at $c_y \approx 0.25$ eV, these two nodes meet at M and annihilate. This process is shown in figure 6.

The existence of these Weyl points was confirmed by verifying that the nodes are a source or a sink of Berry curvature. For this purpose, the Chern number of spheres surrounding the points was calculated by tracking the hybrid Wannier charge centers (HWCCs) on loops around the sphere [2, 37, 40, 41], using the Z2Pack software [37]. Figure 7 shows the evolution of the sum of the HWCC for two of the four nodes found at $c_y = 0.12$ eV, demonstrating that the two points are Weyl nodes of opposite chirality.

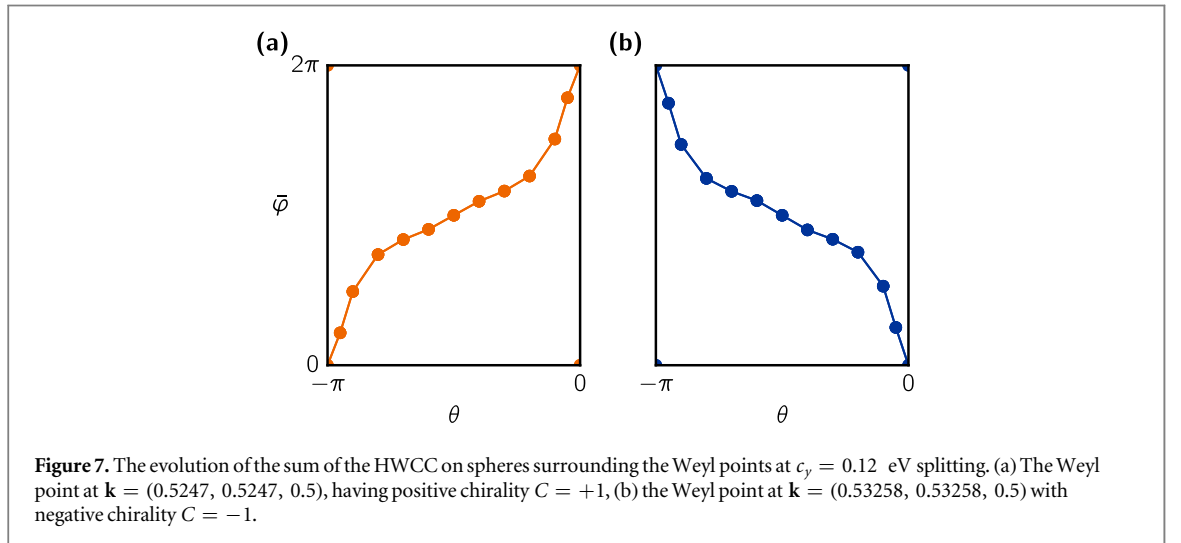
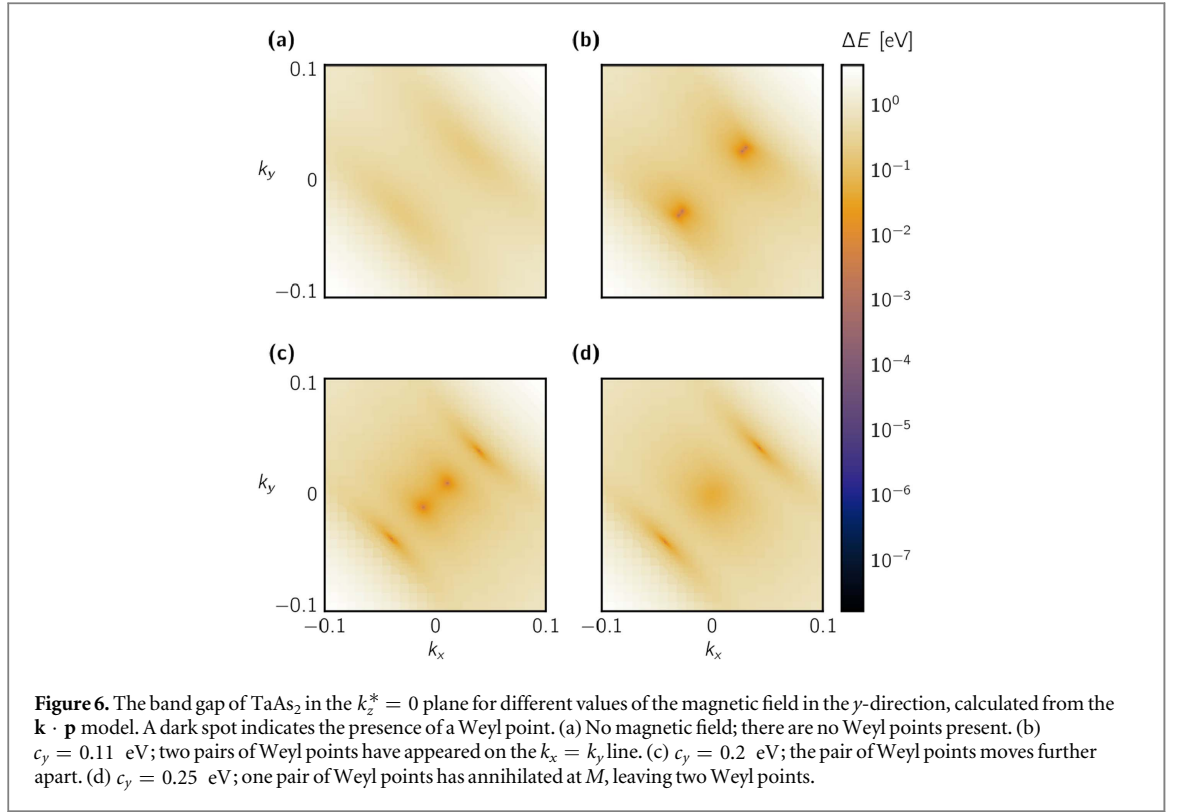
3.2.2. General magnetic field direction

Finally, the effects of a magnetic field in a general direction were studied. It turns out that even though such a field breaks the spatial symmetries of the system, Weyl nodes still appear under a strong enough magnetic field. When a magnetic field is applied in an \hat{x} - or \hat{z} -direction, a single pair of Weyl points emerges from the M -point. These Weyl nodes are located on the $k_x = -k_y$ plane, as shown in table 5.

Figure 8 shows the number of Weyl points as a function of the Zeeman splitting. To obtain this phase diagram, the candidate Weyl points were identified using a quasi-Newton algorithm to find the minima in the band gap (using `SciPy.optimize.minimize` [36]), for different initial guesses. In the second step, the Chern number on the small sphere (radius 10^{-4} Å⁻¹) surrounding the candidate points was evaluated (using Z2Pack [37]), keeping only the points with a non-zero Chern number. Finally, duplicate points were eliminated by checking whether two points lie within the diameter of the sphere of one another.

3.3. The effect of Zeeman splitting on the tight-binding model for NbSb₂

Having studied the effects of Zeeman splitting on the $\mathbf{k} \cdot \mathbf{p}$ model for TaAs₂, we now study a more realistic tight-binding model for NbSb₂, derived from a first-principles calculation with hybrid functionals using the



Wannier90 code [42, 43]. NbSb₂ was chosen because it has the smallest direct band gap of the four materials, making it the most promising candidate for hosting Weyl points at realistic magnetic field strength.

The Zeeman splitting for this model can again be expressed by adding the corresponding terms to the Hamiltonian

$$\Delta\mathcal{H} = c_x\sigma_x \otimes \mathbb{I}_{22 \times 22} + c_y\sigma_y \otimes \mathbb{I}_{22 \times 22} + c_z\sigma_z \otimes \mathbb{I}_{22 \times 22}, \quad (17)$$

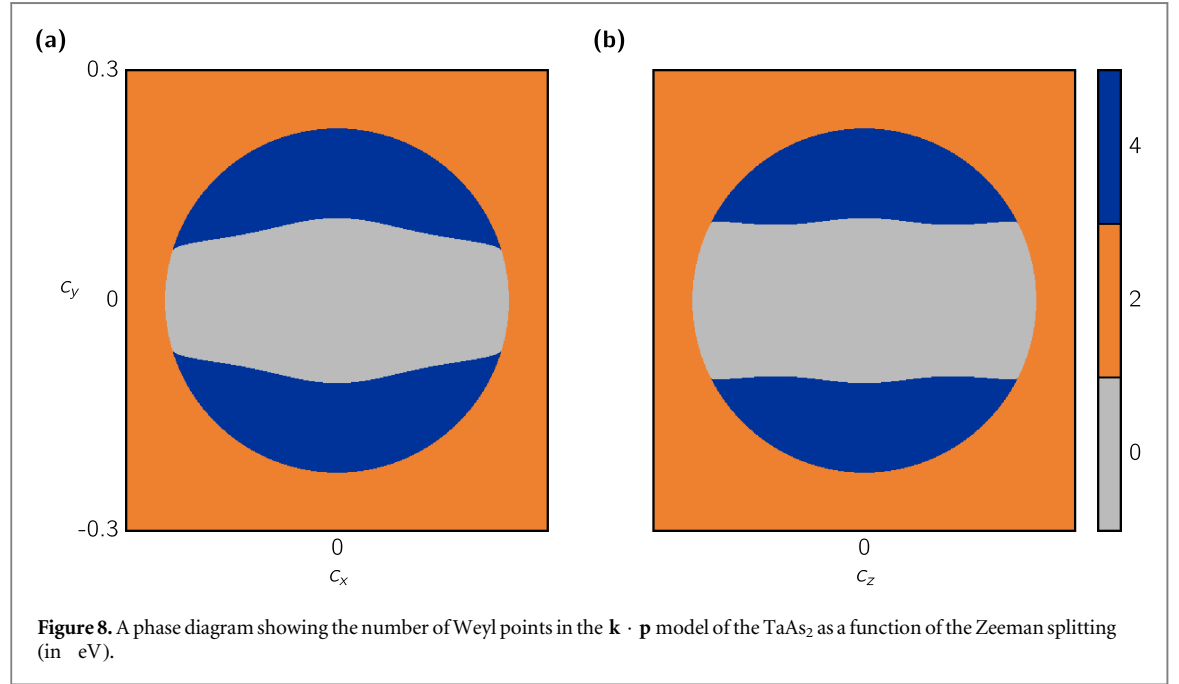
where the change in the splitting terms (compared to equation (13)) is due to the different orbital basis used for the tight-binding model. We search for Weyl points between the last valence band and the first conduction band.

First, we study the effect of applying a magnetic field in the y -direction. Figure 9 shows the effect of this splitting along the $M-A$ line. For $c_y \approx 0.06$ eV, two pairs of Weyl points appear close to the $M-A$ line. The reason these points are not exactly on the line is because the crystal symmetry is broken when constructing the Wannier-based tight-binding model [42, 43]. Apart from the numerical difference, this effect is analogous to the case of the $\mathbf{k} \cdot \mathbf{p}$ model for TaAs₂, where the two pairs of Weyl points appeared at $c_y = 0.11$ eV.

Table 6 shows the Weyl point positions, chirality and type for selected values of Zeeman splitting. It shows that Weyl points appear even at smaller values of c_y away from the $M-A$ line. This is a crucial difference from the

Table 5. The position $\mathbf{k}^* = \mathbf{k} - M$ (in reduced coordinates) and chirality of the Weyl points for Zeeman splitting in the \hat{x} - and \hat{z} -direction.

Splitting [eV]	Weyl position \mathbf{k}^*	Chirality
$c_x = 0.225$	$(-0.0042, 0.0042, 0.00093)$	−1
	$(0.0042, -0.0042, -0.00093)$	1
$c_x = 0.25$	$(-0.025, 0.025, 0.0054)$	−1
	$(0.025, -0.025, -0.0054)$	1
$c_x = 0.3$	$(-0.044, 0.044, 0.0098)$	−1
	$(0.044, -0.044, -0.0098)$	1
$c_z = 0.225$	$(0.0011, -0.0011, -0.018)$	−1
	$(-0.0011, 0.0011, 0.018)$	1
$c_z = 0.25$	$(0.0066, -0.0066, -0.11)$	−1
	$(-0.0066, 0.0066, 0.11)$	1
$c_z = 0.3$	$(0.012, -0.012, -0.18)$	−1
	$(-0.012, 0.012, 0.18)$	1



$\mathbf{k} \cdot \mathbf{p}$ model, which is only valid near the M -point. Furthermore, all Weyl points found for these splitting values are of type-II [2]. Type-II Weyl points have a tilted energy spectrum, making their Fermi surface open instead of point-like. As a consequence, their chiral anomaly—and their effect on magnetoresistance—is expected to be anisotropic.

Finally, a phase diagram was calculated showing the number of Weyl points as a function of the magnetic field (see figure 10). Unlike for the $\mathbf{k} \cdot \mathbf{p}$ model, the number of Weyl points keeps increasing when the applied Zeeman term grows stronger. Again, the reason for this difference is that Weyl points also form far away from the M -point, where the $\mathbf{k} \cdot \mathbf{p}$ approximation is no longer applicable.

For some values of splitting, the phase diagram shows an odd number of Weyl points, which is physically impossible. The reason for this is that the numerical procedure used to identify the number of Weyl points may not find a Weyl point if it is too close to another one. Since this problem only occurs rarely (see figure 11), the phase diagram is still valid overall. Also, the procedure ensures that no Weyl point can be counted twice, so the phase diagram represents a lower limit for the real number of Weyl points. Thus, the general result, in which the number of Weyl points increases with stronger Zeeman splitting, remains valid.

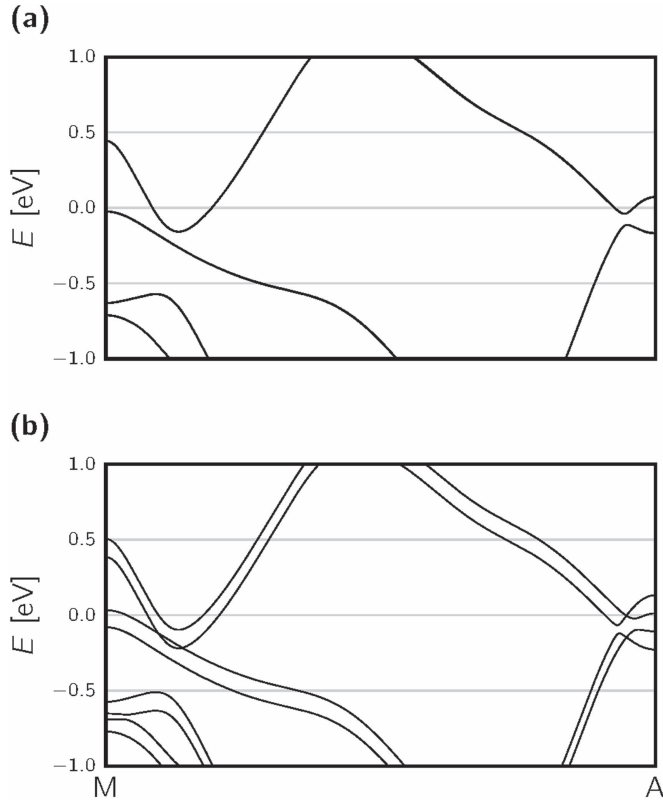


Figure 9. The band structure of the tight-binding model for NbSb₂ along the *M*–*A* line (a) without Zeeman splitting, and (b) with $c_y = 0.06$ eV Zeeman splitting.

3.4. Limitations of the model for the magnetic field

In the previous sections, the effect of the magnetic field was modeled by applying Zeeman splitting to the model Hamiltonian. The discussion was simplified by assuming that the g -factor was equal for all energy bands, and independent of \mathbf{k} . Here, we discuss how the results might change if this assumption is not made.

If the g -factor is k -dependent, but still the same for all energy bands, the results above will change quantitatively, but not qualitatively. The reason for this is that the Weyl node that appears at a specific k -point will still be there, but for a different magnetic field. That is, the order in which the Weyl nodes at different k -points appear might change, but not the overall picture of an increasing number of Weyl points with a stronger magnetic field.

The same is true if the g -factor varies for different energy bands, as long as the sign of the g -factor remains the same. Because the appearance of Weyl points is due to the relative Zeeman splitting between the last valence and first electron bands, it does not matter how much the splitting of each band contributes.

If the g -factors in the relevant bands have opposite signs, however, there is a qualitative change in behavior. This is illustrated in the following with the example of the $\mathbf{k} \cdot \mathbf{p}$ model of TaAs₂, discussed in sections 2.3, 3.2. To account for the opposite sign of the g -factor for the valence and conduction bands, the Zeeman splitting term (equation (13)) is changed to

$$\Delta\mathcal{H} = c_x \sigma_z \otimes \sigma_y + c_y \sigma_z \otimes \sigma_z + c_z \sigma_z \otimes \sigma_x. \quad (18)$$

With c_y splitting, the energy bands on the mirror plane are then given by

$$E(\mathbf{k}) = C_{00}(\mathbf{k}) \pm c_y \mp \sqrt{C_{xx}(\mathbf{k})^2 + C_{xy}(\mathbf{k})^2 + C_{z0}(\mathbf{k})^2}. \quad (19)$$

As in equation (16), the Zeeman term counteracts the original splitting. The difference from the previous case is that this equation holds on an entire plane in reciprocal space instead of just a line. As a consequence, we can expect the appearance of a nodal line with sufficient Zeeman splitting. Indeed, a nodal line appears for $c_y \gtrsim 0.2242$ eV, as shown in figure 12. The Berry phase on a closed path around this nodal line was calculated to be π , using the Z2Pack [37] software. This verifies the topological nature of the nodal line.

In conclusion, the qualitative result obtained above remains intact when the g -factors are assumed to be k -dependent, and different for the valence and conduction bands, as long as they keep the same sign. A more adequate model of the magnetic field is needed to establish the exact qualitative and quantitative nature of the

Table 6. The Weyl point positions (in reduced coordinates), chirality and type for different values of Zeeman splitting in the tight-binding model for NbSb₂.

Splitting [eV]	Position k	Chirality	Type
$c_x = 0.045$	(0.4393, 0.4460, 0.5004)	+1	II
	(0.4359, 0.4444, 0.5026)	-1	II
	(0.5641, 0.5556, 0.4974)	+1	II
	(0.5607, 0.5540, 0.4996)	-1	II
$c_y = 0.03$	(0.3670, 0.5141, 0.0977)	+1	II
	(0.3655, 0.5142, 0.1004)	-1	II
	(0.6345, 0.4858, 0.8997)	+1	II
	(0.6330, 0.4858, 0.9023)	-1	II
$c_y = 0.04$	(0.3724, 0.5116, 0.0890)	+1	II
	(0.3627, 0.5135, 0.1055)	-1	II
	(0.6373, 0.4865, 0.8945)	+1	II
	(0.6276, 0.4884, 0.9110)	-1	II
	(0.9028, 0.0340, 0.5451)	+1	II
	(0.9018, 0.0354, 0.5390)	-1	II
	(0.0982, 0.9646, 0.4610)	+1	II
	(0.0974, 0.9658, 0.4545)	-1	II
$c_y = 0.06$	(0.3791, 0.5068, 0.0775)	+1	II
	(0.3592, 0.5131, 0.1108)	-1	II
	(0.6407, 0.4869, 0.8892)	+1	II
	(0.6211, 0.4929, 0.9222)	-1	II
	(0.9033, 0.0328, 0.5532)	+1	II
	(0.9006, 0.0364, 0.5314)	-1	II
	(0.0994, 0.9636, 0.4686)	+1	II
	(0.0968, 0.9671, 0.4467)	-1	II
	(0.4493, 0.4555, 0.5031)	+1	II
	(0.4309, 0.4320, 0.4825)	-1	II
	(0.5691, 0.5680, 0.5175)	+1	II
	(0.5507, 0.5445, 0.4969)	-1	II
$c_z = 0.0475$	(0.4494, 0.4384, 0.4853)	+1	II
	(0.4420, 0.4366, 0.4816)	-1	II
	(0.5580, 0.5634, 0.5184)	+1	II
	(0.5506, 0.5616, 0.5147)	-1	II

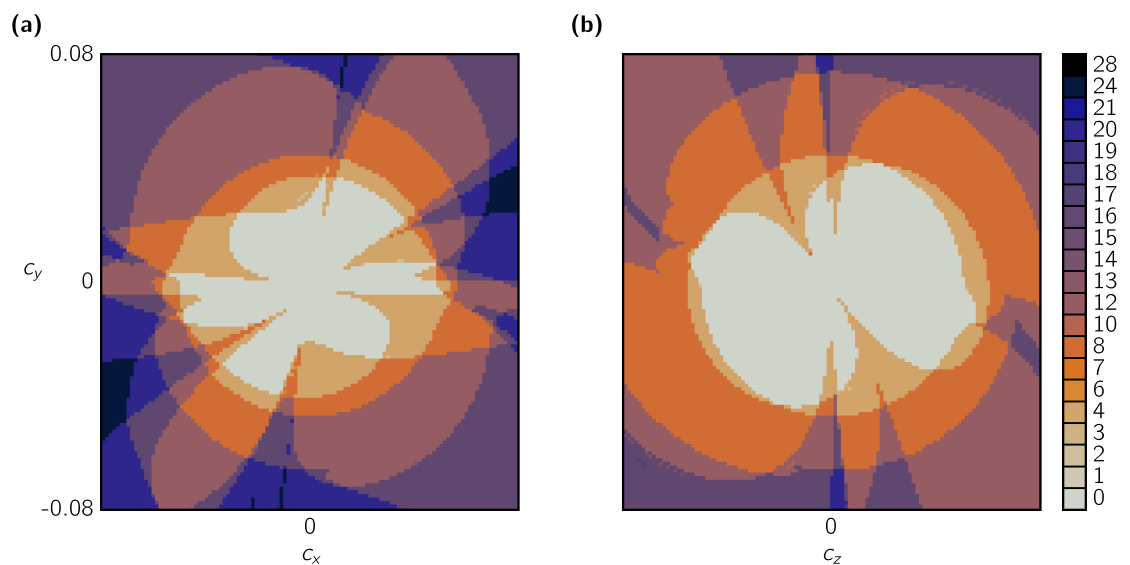
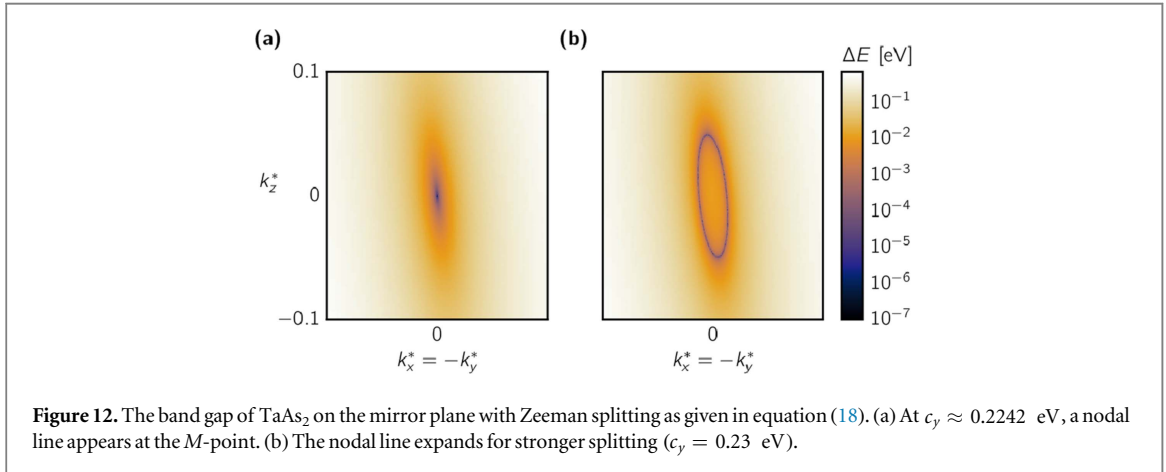
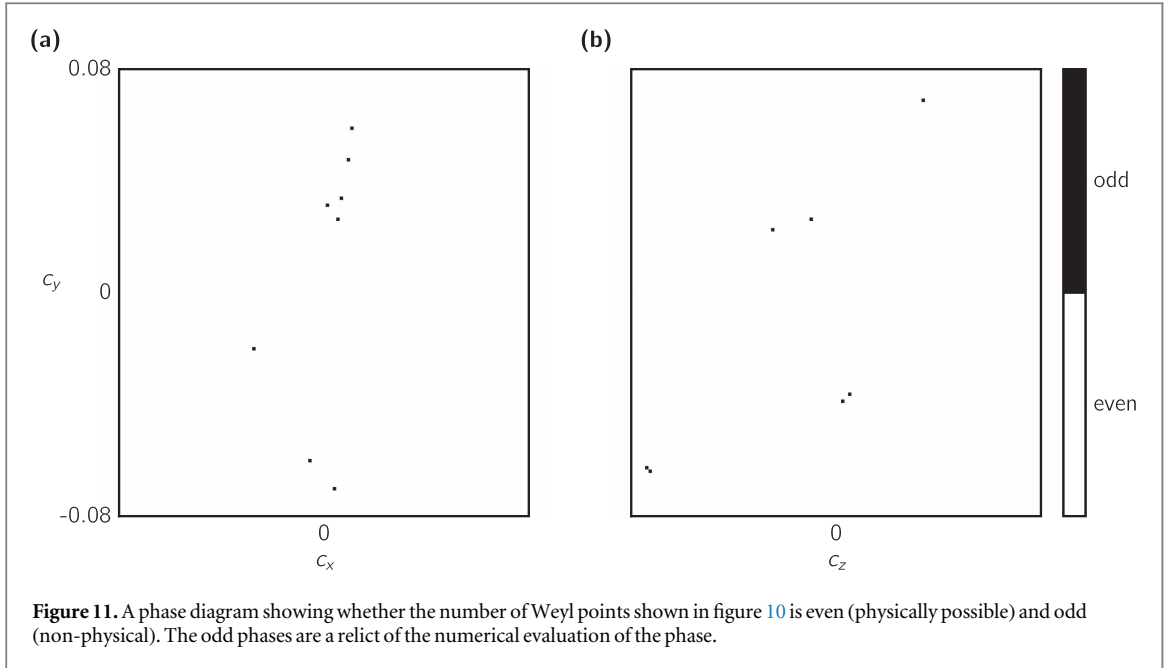


Figure 10. The phase diagram showing the number of Weyl points as a function of Zeeman splitting (in eV) for the tight-binding model for NbSb₂.



topological phases with the applied magnetic field. The current results indicate that Weyl nodes will appear, at least for some directions of magnetic field.

4. Conclusions

We studied the topological phase of transition metal dipnictides of the type AB₂ ($A \in \{\text{Ta}, \text{Nb}\}$, $B \in \{\text{As}, \text{Sb}\}$), with and without an external magnetic field. In the absence of a magnetic field, we found—in accordance with previous results [15, 17]—that these materials can be classified as weak topological insulators, despite having an indirect band gap closure.

The effect of the magnetic field was studied by applying Zeeman splitting, and we found that Weyl points can appear. We showed this result first from theoretical considerations on a four-band $\mathbf{k} \cdot \mathbf{p}$ model, and numerically on a $\mathbf{k} \cdot \mathbf{p}$ model of TaAs₂ and a tight-binding model of NbSb₂. In the tight-binding model, we found the number of Weyl points to increase with a growing magnetic field. For specific values of Zeeman splitting, the type of Weyl points in the tight-binding model was studied, and they were all found to be of type-II.

The appearance of such field-induced Weyl points could help explain the reduced or negative magnetoresistivity in these materials. However, it is unclear whether the Weyl points studied here appear at a magnetic field that is realistic to observe in experiments. Further studies, in particular, to obtain a realistic g -factor and more reliable data for the direct band gap, are required to accurately estimate the required magnetic field. Furthermore, it is known that modeling a strong magnetic field with only Zeeman splitting is not sufficient, and a more accurate model should be considered. Finally, the effect of these Weyl points on the

magnetoresistance should be calculated. This is influenced by the orientation of the type-II Weyl points, and their distance from the Fermi level.

Consequently, there are three open questions which require further investigation: first, whether the appearance of field-induced Weyl points is realistic in these AB₂ compounds; second, if these Weyl points do appear, whether they alone are responsible for the experimentally observed behavior of magnetoresistance or if there are other effects; finally, whether there are other compounds which contain the same kind of field-induced Weyl points, possibly appearing already at a weaker magnetic field.

Acknowledgments

We would like to thank D Rodic and M Könz for helpful discussions. The authors were supported by ERC Advanced Grant SIMCOFE, Microsoft Research, and the Swiss National Science Foundation through the National Competence Centers in Research MARVEL and QSIT. Calculations were performed on the Mönch cluster of ETH Zurich.

References

- [1] Volovik G E 1987 Zeros in the Fermion spectrum in superfluid systems as diabolical points *JETP Lett.* **46** 98–102
- [2] Soluyanov A A, Gresch D, Wang Z, Wu Q, Troyer M, Dai X and Andrei Bernevig B 2015 Type-II Weyl semimetals *Nature* **527** 495–8
- [3] Adler L S 1969 Axial-vector vertex in spinor electrodynamics *Phys. Rev.* **177** 2426–38
- [4] Bell J S and Jackiw R 1969 A PCAC puzzle: $\pi^0 \rightarrow \gamma\gamma$ in the σ -model *Nuovo Cimento* **60** 47–61
- [5] Nielsen H B and Ninomiya M 1983 The Adler-Bell-Jackiw anomaly and Weyl Fermions in a crystal *Phys. Lett. B* **130** 389–96
- [6] Abrikosov A A 1998 Quantum magnetoresistance *Phys. Rev. B* **58** 2788
- [7] Son D T and Spivak B Z 2013 Chiral anomaly and classical negative magnetoresistance of Weyl metals *Phys. Rev. B* **88** 104412
- [8] Huang X et al 2015 Observation of the chiral-anomaly-induced negative magnetoresistance in 3D Weyl semimetal TaAs *Phys. Rev. X* **5** 031023
- [9] Xiong J, Kushwaha S K, Liang T, Krizan J W, Hirschberger M, Wang W, Cava R J and Ong N P 2015 Evidence for the chiral anomaly in the Dirac semimetal Na₃Bi *Science* **350** 413–6
- [10] Arnold F et al 2016 Negative magnetoresistance without well-defined chirality in the Weyl semimetal TaP *Nature Comm* **7**
- [11] Yang X, Liu Y, Wang Z, Zheng Y and Xu Z-A 2015 Chiral anomaly induced negative magnetoresistance in topological Weyl semimetal NbAs arXiv:1506.03190
- [12] Wang K, Graf D, Li L, Wang L and Petrovic C 2014 Anisotropic giant magnetoresistance in NbSb₂ *Sci. Rep.* **4** 7328
- [13] Wang Y-Y, Yu Q-H, Guo P-J, Liu K and Xia T-L 2016 Resistivity plateau and extremely large magnetoresistance in NbAs₂ and TaAs₂ *Phys. Rev. B* **94** 041103
- [14] Wu D et al 2016 Giant semiclassical magnetoresistance in high mobility TaAs₂ semimetal *Appl. Phys. Lett.* **108** 042105
- [15] Luo Y, McDonald R D, Rosa P F S, Scott B, Wakeham N, Ghimire N J, Bauer E D, Thompson J D and Ronning F 2016 Anomalous electronic structure and magnetoresistance in TaAs₂ *Sci. Rep.* **6** 27294
- [16] Yuan Z, Lu H, Liu Y, Wang J and Jia S 2016 Large magnetoresistance in compensated semimetals TaAs₂ and NbAs₂ *Phys. Rev. B* **93** 184405
- [17] Li Y, Wang Z, Lu Y, Yang X, Shen Z, Sheng F, Feng C, Zheng Y and Xu Z-A 2016 Negative magnetoresistance in topological semimetals of transition-metal dipnictides with nontrivial \mathbb{Z}_2 indices arXiv:1603.04056
- [18] Shen B, Deng X, Kotliar G and Ni N 2016 Fermi surface topology and negative longitudinal magnetoresistance observed in the semimetal NbAs₂ *Phys. Rev. B* **93** 195119
- [19] Wang Z, Li Y, Lu Y, Shen Z, Sheng F, Feng C, Zheng Y and Xu Z 2016 Topological phase transition induced extreme magnetoresistance in TaSb₂ arXiv:1603.01717
- [20] Li Y, Li L, Wang J, Wang T, Xu X, Xi C, Cao C and Dai J 2016 Resistivity plateau and negative magnetoresistance in the topological semimetal TaSb₂ *Phys. Rev. B* **94** 121115
- [21] Cano J, Bradlyn B, Wang Z, Hirschberger M, Ong N P and Bernevig B A 2016 *The chiral anomaly factory: Creating Weyls with a magnetic field* arXiv:1604.08601
- [22] Ling R G and Belin C 1981 Affinement de la structure cristalline du diarseniure de tantale *CR Acad. Sci. Paris* **292** 891–3
- [23] Hulliger F 1964 New representatives of the NbAs₂ and ZrAs₂ structures *Nature* **204** 775
- [24] Lomnytska Y F and Berezovets V V 2005 Phase relations in the Nb-Ni-Sb system *Inorg. Mater.* **41** 1166–71
- [25] Bensch W and Heid W 1995 NbAs₂ *Acta Crystallogr.* **51** 2205–7
- [26] Kresse G and Furthmüller J 1996 Efficiency of ab-initio total energy calculations for metals and semiconductors using a plane-wave basis set *Comput. Mater. Sci.* **6** 15–50
- [27] Blöchl P E 1994 Projector augmented-wave method *Phys. Rev. B* **50** 17953
- [28] Kresse G and Joubert D 1999 From ultrasoft pseudopotentials to the projector augmented-wave method *Phys. Rev. B* **59** 1758
- [29] Perdew J P, Burke K and Ernzerhof M 1996 Generalized gradient approximation made simple *Phys. Rev. Lett.* **77** 3865
- [30] Heyd J, Scuseria G E and Ernzerhof M 2003 Hybrid functionals based on a screened Coulomb potential *J. Chem. Phys.* **118** 8207–15
- [31] Krukau A V, Vydrov O A, Izmaylov A F and Scuseria G E 2006 Influence of the exchange screening parameter on the performance of screened hybrid functionals *J. Chem. Phys.* **125** 224106
- [32] Xu C, Chen J, Zhi G-X, Li Y, Dai J and Cao C 2016 Electronic structures of transition metal dipnictides XPn₂ (X = Ta, Nb; Pn = P, As, Sb) *Phys. Rev. B* **93** 195106
- [33] Kostert G F, Dimmock J O, Wheeler R G and Statz H 1963 *Properties of the Thirty-two Point Groups* 24 (Cambridge, MA: MIT Press)
- [34] Blaha P, Schwarz K, Madsen G K H, Kvasnicka D and Luitz J 2001 WIEN2k *Technical Universität Wien Austria*
- [35] Schwarz K, Blaha P and Madsen G K H 2002 Electronic structure calculations of solids using the WIEN2k package for material sciences *Computer Phys. Comm.* **147** 71–6
- [36] Jones E et al 2001 SciPy: Open Source Scientific Tools for Python (Accessed: 2015-05-26)

- [37] Gresch D, Autès G, Yazyev O V, Troyer M, Vanderbilt D, Bernevig B A and Soluyanov A A 2016 Z2Pack: Numerical implementation of hybrid Wannier centers for identifying topological materials arXiv:1610.08983
- [38] Sancho M P L, Sancho J M L, Sancho J M L and Rubio J 1985 Highly convergent schemes for the calculation of bulk and surface Green functions *J. Phys. F: Met. Phys.* **15** 851
- [39] Wu Q G and Zhang S N 2015 *Wannier Tools* https://github.com/quanshengwu/wannier_tools
- [40] Wang Z, Gresch D, Soluyanov A A, Xie W, Kushwaha S, Dai X, Troyer M, Cava R J and Bernevig B A 2016 MoTe₂: a type-II Weyl topological metal *Phys. Rev. Lett.* **117** 056805
- [41] Autès G, Gresch D, Troyer M, Soluyanov A A and Yazyev O V 2016 Robust type-II Weyl semimetal phase in transition metal diphosphides XP₂ (X = Mo, W) *Phys. Rev. Lett.* **117** 066402
- [42] Mostofi A A, Yates J R, Lee Y-S, Souza I, Vanderbilt D and Marzari N 2008 wannier90: A tool for obtaining maximally-localised Wannier functions *Computer Phys. Comm.* **178** 685–99
- [43] Mostofi A A, Yates J R, Pizzi G, Lee Y-S, Souza I, Vanderbilt D and Marzari N 2014 An updated version of wannier90: a tool for obtaining maximally-localised Wannier functions *Computer Phys. Comm.* **185** 2309–10